Received: 12 February 2021 | Revised: 27 August 2021 | Accepted: 15 October 2021

DOI: 10.1111/jfr3.12770

ORIGINAL ARTICLE

CIWEM Chartered Institution of Water and Environmental Management | Journal of Flood Risk Management | WILEY

Country-wide flood exposure analysis using Sentinel-1 synthetic aperture radar data: Case study of 2019 Iran flood

Sonam Futi Sherpa | **Manoochehr Shirzaei**

Department of Geosciences, Virginia Tech, Blacksburg, Virginia, USA

Correspondence
Sonam Futi Sherpa, Department of Geosciences, Virginia Tech, Derring Hall, Blacksburg, VA 24060, USA.
Email: sfsherpa@vt.edu

Funding information
National Aeronautics and Space Administration, Grant/Award Number: 80NSSC170567

Abstract

Extreme precipitation and flooding often lead to human and economic losses. However, the high-resolution nationwide flooding exposure data are scarce. Availability of all-weather space-borne SAR satellite data can potentially improve the ability to generate high-resolution flood map extent and exposure globally. In Iran, flooding is a major concern, given the socioeconomic vulnerabilities and increased likelihood of climate extremes. Iran experienced extreme flooding during January to March 2019, attributed to significant precipitation during October 2018 to March 2019, which is well above the long-term averages for 1999–2019. Using Pettitt and Mann Kendall tests, nationwide precipitation records were identified by significant decreasing and increasing trends in north and south, respectively. Utilizing 673 Sentinel-1 SAR intensity images, we applied a fast-marching algorithm for image segmentation in combination with a Bayesian framework to obtain high-resolution probabilistic flood maps. We found, 22, 9, and 15 states in January, February, and March, respectively, experienced flooding that covered >15% of their area with high flooded area percent in the northwestern and southeastern region. We estimated that >15, >11.32, and >11.33 million people were exposed to floods in January, February, and March, respectively. Our datasets inform flooding models and management efforts under increasing climate extremes and changing land use and cover.

KEYWORDS

2019 Iran flood, fast marching algorithm, precipitation analysis, probabilistic flood map exposure, synthetic aperture radar (SAR)

1 | INTRODUCTION

Changes in frequency, intensity, and timing of extreme climate events, causing disasters, are associated with changing climate (AghaKouchak et al., 2020; Dottori et al., 2018; Shukla et al., 2019). Several studies have reported an increased frequency of extreme rainfall events over the past decades (Coumou & Rahmstorf, 2012; Taylor et al., 2017). They have projected a future increase in such events due to elevated global temperature, which in turn leads to an increase in flooding frequencies, primarily due to an increase in heavy rain days, though the total rainfall is decreasing (Dottori et al., 2018; Hirabayashi et al., 2008).

Hirabayashi et al. (2021) suggested that projected potential global exposure to flooding is proportional to the degree of warming, leading to a more significant threat given the climate models. Moreover, Sixth Assessment Report (AR6) by the Intergovernmental Panel on Climate Change (IPCC) stated that the heavy precipitation events would become more frequent and intense than in the recent past on a global and continental scale and translates to an increase in frequency and magnitude of pluvial floods such as surface water and flash floods with a high degree of confidence (Seneviratne et al., 2021). Further, various studies have also highlighted the influence of anthropogenic and geomorphological factors such as the role of land use and land cover changes on flooding, flood intensification, and losses, in addition to hydrometeorological factors (Adnan et al., 2020; Rahman et al., 2021; Rogger et al., 2017; Roy et al., 2020; Saghafian et al., 2008). Flood changes at a catchment scale could be caused by changes in forest management, agricultural practices, and infrastructural developments (Hajian et al., 2019; Pal et al., 2021; Rogger et al., 2017).

Such increased frequency of severe flooding, linked to anthropogenically driven climate change, the influence of anthropogenic factors, combined with growing world population, has exacerbated the socioeconomic vulnerability and exposure (Hirabayashi et al., 2021; Intergovernmental Panel on Climate Change, 2014; Wallemacq, 2018; Willis et al., 2016; Wobus et al., 2014; Yamazaki et al., 2018). To develop resilience plans and mitigation strategies, hindcast exposure models, and calculate the insurance payouts, accurate maps of flooding extent and socioeconomic exposure at management, relevant resolution (10^2 m) are needed.

In January to March 2019, Iran experienced one of its most severe precipitation and flooding. The 2019 flood of Iran, causing $5.4 billion worth of damage, ranked the second most expensive flood in Iranian history, after the floods of April to June 1992, according to the International Disaster Database (www.emdat.be). The death toll of the 2019 flood is also ranked as the 18th deadliest flood in Iranian history. Iran's population is expected to surpass 90 million by 2030 (United Nations, 2019) from the current population of 80 million (Figure 1a), highlighting the increased vulnerability and exposure to future extreme climate events. Although we do not have a definitive answer to how changing climates may impact flooding events such as that of 2019 Iran, a recent study suggests that Iran is likely to experience more extended periods of extreme temperature or precipitation in the future and total rainfall of more than 110 mm in three consecutive days, leading to more flooding (Vaghefi et al., 2019).

In an average meteorological year of Iran, three-quarters of Iran's rain falls between December and March. Two main factors act in condition to concentrate the rainfall, leading to disastrous flooding. Firstly, both the Zagros mountains running across southwest Iran and the Alborz mountains in the northeast act as barriers to airflow, keeping the center of the country dry as the rain is deposited on the windward side of the country high ground. Secondly, the inability of rainfall to penetrate the ground due to a combination of land use, soil type, and terrain characterized by steep-sided valleys, causing flash flooding (Vaghefi et al., 2019). Approximately six significant floods occurred in arid and semiarid parts of the country, which was not expected (Floodlist, 2018). Hajian et al. (2019), highlighted that even in the absence of deforestation (land use and land cover change), climate change such as extreme rainfall presents a significant flood hazard in the northern province of Iran in the perimeter of the Caspian Sea. Further, given the geophysical conditions and other factors, flooding is considered the second most common natural hazard after earthquakes (World Bank, 2019).

Data provided by earth-observing synthetic aperture radar (SAR) satellites enables mapping the disaster extent in semi-real-time with a higher resolution and is of great importance for flood exposure analysis and mitigation efforts and future hazards assessments and management. This is due to SAR sensors' all-weather day and night image acquisition abilities and broad spatial coverage, frequency, and repeat intervals (Alvan Romero et al., 2020; Clement et al., 2018; Sherpa et al., 2020). Unlike other space-based techniques such as optical satellites, SAR works as a significant resource for inundation mapping even in the presence of clouds, which is often the case, especially during compound events such as extreme rainfall and flooding. Based on the backscattering intensity of the SAR image where water appears as a dark area resulting in a low backscatter recording as incident radar signals are reflected away from the radar antenna (Henderson & Lewis, 1998), one can visualize and interpret flooding based on various classification methods. This includes a simple visual interpretation approach (Matgen et al., 2007; Oberstadler et al., 1997; Sanyal & Lu, 2004), image change detection (Bazi et al., 2005; Clement et al., 2018; Nico et al., 2000), region growing algorithms (Malnes et al., 2002; Mason et al., 2012), supervised classification (Pulvirenti et al., 2013; Townsend, 2002), histogram thresholding (Chini et al., 2012; Elkhrachy et al., 2021; Pulvirenti et al., 2016), and clustering algorithm (Ruzza et al., 2019). Further, many flood detection approaches have used a combination of thresholding, region growing, and change detection utilizing a single SAR image (Giustarini et al., 2016; Matgen et al., 2011). A more robust approach for estimating flood extent is developed by Chini

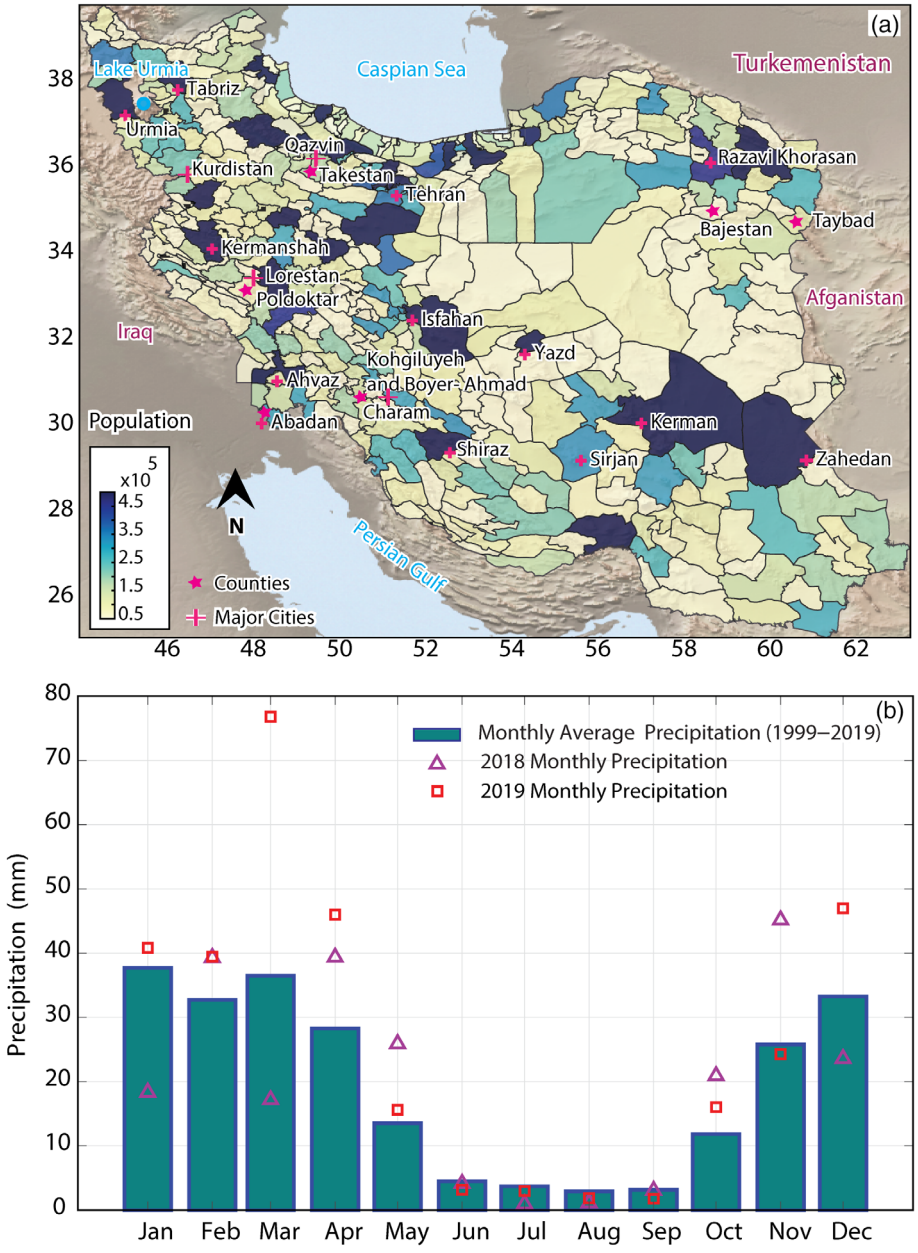

FIGURE 1 (a) Iran study area with its population distribution at the county level (Source: data.humdata.org). Major cities are highlighted in magenta cross color. (b) Monthly averaged precipitation for 1999–2019 (green bar) aggregated over Iran. Also shown are monthly precipitation of the year 2018 (triangle) and year 2019 (square) (Source: https://pmm.nasa.gov/data-access/downloads/trmm)

et al. (2017) using the hierarchical split-based approach to obtain the distribution of flooded and non-flooded pixels building on the works of Matgen et al. (2011). The hierarchical split-based approach is also utilized in Sherpa et al. (2020).

Recent flood mapping algorithms are concerned with probabilistic mapping of flood extent instead of a binary approach that provides no information on the uncertainty of pixels' flooding condition (Giustarini et al., 2016). Studies have highlighted various sources of uncertainty for a single SAR image and associated flooding extent map, such as (i) classification threshold value to determine a pixel as a flooded or non-flooded, (ii) uncertainty due to partial flooding of a pixel, (iii) geocoding of images (Schumann et al., 2008), and (iv) uncertainty that derives from speckles (Giustarini et al., 2015). Here we addressed all the error sources mentioned above, but the uncertainty due to partial pixel flooding concerns the probabilistic approaches of flooding mapping and exposure analysis. Such flood extent maps with uncertainty are useful for data assimilation where uncertainties associated with observations have to be quantified to ensure optimal use of the assimilation filters required by flood managers and insurance companies and related agencies as it reflects the level of confidence that can be attributed to the mapped flood extent (Giustarini et al., 2016). Here, we apply a statistical approach based on the Bayes theorem, in which each pixel is characterized by a probability indicating the likelihood of the pixel being flooded. To set up the Bayesian

framework and obtain marginal probability density functions of flooded and non-flooded pixels, we implement a fast-marching algorithm for SAR image segmentation (Sethian, 1999). The presented framework here is a semisupervised approach, scalable to a regional and global scale with minimal effort. These maps are a low-cost resource for rapid response efforts and evaluating hazards impact, provided that vast SAR datasets from civil and commercial satellites are becoming available (Rosen, 2021).

To assess the long-term trends and changes in climatic conditions, we further investigated the non-stationarity of the time series of space-based precipitation data from TRMM multisatellite precipitation analysis (TMPA) by observing the presence of abrupt changes in the mean as well as the monotonic trends. We performed two statistical tests, including Pettitt (Pettitt, 1979) and Mann–Kendall tests (Kendall, 1975; Mann, 1945). The rationale behind this is that if there is a statistically significant trend in the time series, it may persist into the future, providing clues for the frequency of repeating a flooding-type similar to that observed through 2019.

We use an available population database to evaluate the flooding exposure at the county and state levels. At a national and global scale, flood exposure analysis is usually performed using global scale population density data and hydrodynamic flood models (Bates et al., 2010; Neal et al., 2012; Smith et al., 2019; Tiecke et al., 2017). However, large-scale studies using high-resolution direct observation of the flood extent, such as those provided by SAR, are scarce. Thus, such probabilistic flood map and exposure are essential for determining the socioeconomic flood exposure for better risk management, developing long-term resiliency plans, and data assimilation, which is found to significantly improve the prediction of streamflow and water level (Di Mauro et al., 2021; Scotti et al., 2020). Further, this study also highlights the importance of earth-observing SAR data sets with open-access policy, such as Sentinel and future NASA-ISRO SAR (NISAR) mission, for rapid disaster response, where field observations are not available due to severe weather conditions and the broad extent of the affected area.

2 | DATA

2.1 | Precipitation data

To investigate the precipitation pattern in the study area, we use the National Aeronautics and Space Administration (NASA) version 7 of TRMM Multisatellite Precipitation Analysis daily level 3 data (Huffman et al., 2007, 2010). We used the "Precipitation (mm/hr)" product from January 1, 1999 to December 31, 2019 at a resolution of $0.25^\circ \times 0.25^\circ$. Further details of this data product can be found in Kummerow et al. (1998). Darand et al. (2017) showed the usefulness of the TRMM product over Iran and specifically where rain gauge observation is sparse and concluded that the spatial and temporal variations of precipitation are well captured by the multisatellite product TRMM products over Iran. Since our analysis was over the entire country, we utilized the TRMM product for precipitation analysis purposes.

The monthly average precipitation from 1999 to 2019 and the 2018 and 2019 monthly precipitations are shown in Figure 1b. In 2019, most non-summer months experienced precipitation higher than the 20-year average, with a peak in March whose value is twice the average. Further, monthly total precipitation aggregated over state and counties of Iran for January, February, and March 2019 are shown in Figure 2. The northwest part of the country experienced more precipitation in all 3 months, with the highest in March (Figure 2) at both county and state levels.

2.2 | Synthetic aperture radar (SAR) data

We obtained and analyzed the full archive of SAR images, totaling 686 scenes, acquired by Sentinel-1 C-Band Satellite from European Space Agency with a temporal sampling of 12 days from January 1 to the end of March (namely, 20190104141633 through 20190331145156, with name formatting of YYYYMMDDhhmmss and hhmmss denoting the Coordinated Universal Time) to map the extent of 2019 Iran flood. We use Gamma software (Urs et al., 2000; Wegnüller et al., 2016) for SAR data processing, including single look complex (SLC) generation, radiometric calibration, and co-registration. We applied multilooking factors of 30 and 5 in range and azimuth to obtain a pixel resolution of $\sim 70 \times 70$ m. The coarse co-registration is performed using satellite ephemeris data and a reference Shuttle Radar Topographic Mission (SRTM) DEM at 30-m resolution (Farr et al., 2007). Next, an enhanced spectral diversity is applied for precisely align SAR images at sub-pixel precision (Shirzaei et al., 2017).

For our flood mapping, we used the amplitude of the SAR images. In the case of smooth water, the incident radar signal is reflected away from the satellite (Henderson & Lewis, 1998). Therefore, in a single SAR log-transformed amplitude image, the smooth open water appears as a dark area and has a low backscattering recording. On the other hand, the non-flooded area and terrain backscatter the signal in many directions and result in a brighter intensity recording.

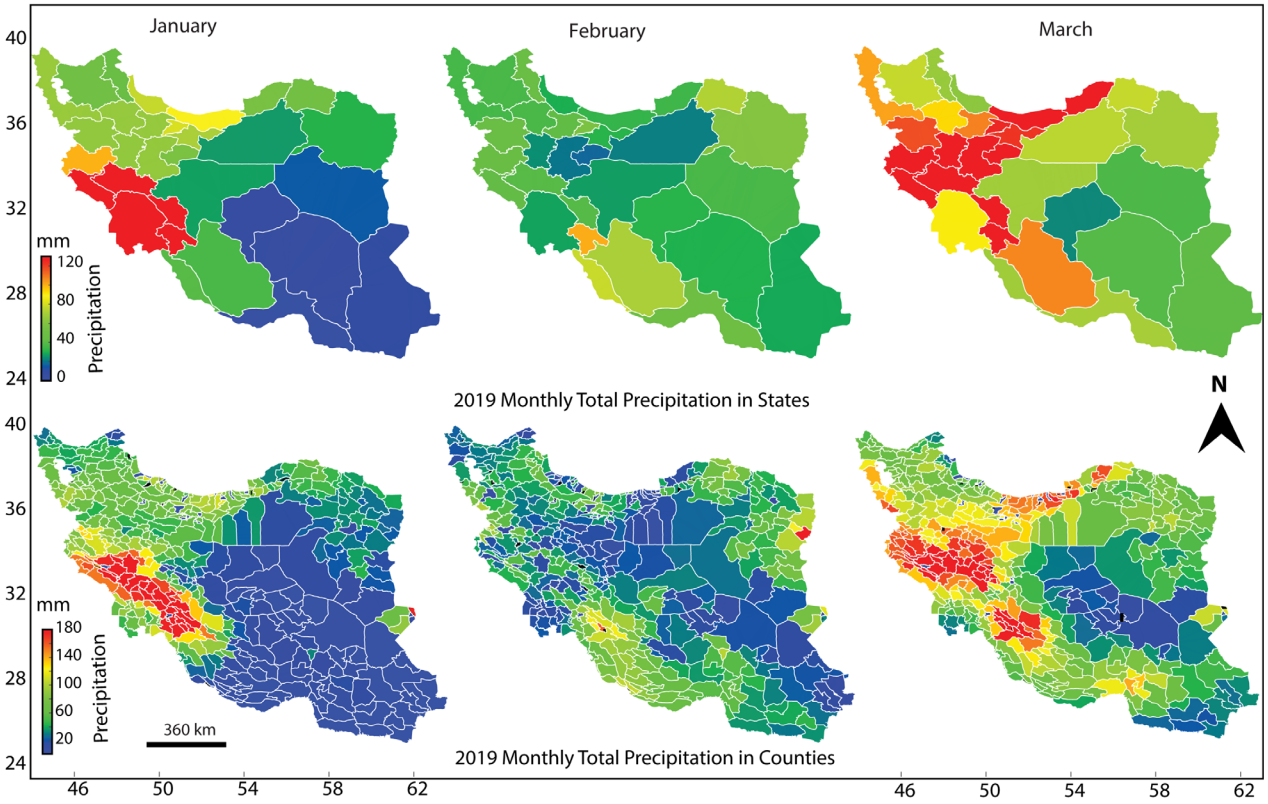

FIGURE 2 Monthly total precipitation aggregated over states (a) and counties (b) of Iran for January, February, and March 2019. Note that the color bars in the panel (a) and (b) are different

3 | METHODS

3.1 | Non-stationarity analysis

We examined the non-stationarity of the monthly precipitation time series data from 1999 to 2019 using TRMM data to evaluate if the rainfall variable consistently increases (decreases) through time using monthly datasets. We applied statistical tests to detect the presence of abrupt changes in the mean and a trend, as discussed in the following.

A nonparametric Pettitt's test (Pettitt, 1979) was applied to detect the monthly level change points. This test is rank-based and evaluates the null hypothesis (H_0), at which the rainfall variable follow one or more distributions with identical parameters, namely, the mean of a time series does not change, against the alternative hypothesis (H_1), at which there is a change point where variables distribution alters. Numerous studies have used this test to analyze annual and seasonal rainfall and discharge maxima (Bodian et al., 2020; Ouhamdouch & Bahir, 2017; Serinaldi & Kilsby, 2014; Villarini & Vecchi, 2012). Applying Pettitt's test to precipitation data, we were able to detect change points.

Furthermore, trends in the time series of precipitation were analyzed using the Mann–Kendall test (Kendall, 1975; Mann, 1945). The Mann–Kendall test statistically assesses the presence of a significant rising or falling trend in a time series, but the trend may or may not be linear. Such nonparametric tests, which are determined by the ranks and sequences of time series rather than original values, can handle non-normally distributed datasets and are less sensitive to data gaps (Hirsch & Slack, 1984) and outliers (Hamed, 2008), which are very common in hydrometeorological time series (Dong et al., 2019; Duan et al., 2019; Gao et al., 2019). Mann–Kendall test is broadly used to analyze various hydrological and meteorological observations (Serinaldi & Kilsby, 2015; Villarini, 2012; Villarini et al., 2011; Villarini & Vecchi, 2012). Here, the test evaluated the null hypothesis (H_0) that no significant trend (upward or downward) exists in the monthly rainfall data, assuming independent data with the identical distribution. For this study, all the statistical significances are tested at three levels 0.01, 0.05, and 0.1.

3.2 | Probabilistic flood mapping

We applied a Bayesian framework to SAR intensity images to calculate the probability of a SAR pixel being flooded (Giustarini et al., 2016; Sherpa et al., 2020), for which a likelihood probability density function was

estimated, thereby providing a continuous value between 0 and 1 as a probabilistic flood map.

The conditional probability of a pixel being flooded for a log-transformed SAR image denoted as $p(F|\sigma^0)$ is given by

$$p(F|\sigma^0) = \frac{p(\sigma^0|F)p(F)}{p(\sigma^0)} \quad (1)$$

$$p(\sigma^0) = p(\sigma^0|F)p(F) + p(\sigma^0|\overline{F})p(\overline{F}) \quad (2)$$

where, σ^0 is log-transformed backscattering intensity, $p(\sigma^0|F)$ denotes the probability of recording a given backscatter value σ^0 for a water pixel (F) and $p(\sigma^0|\overline{F})$ is the probability of recording a given backscatter value σ^0 for a non-water pixel ($\overline{F}$). Also, $p(\sigma^0)$ is the marginal probability of recording a given backscatter value σ^0 for any pixel. The terms $p(F)$ and $p(\overline{F})$ are the prior probabilities of a pixel being flooded and non-flooded, respectively. As the posterior probability distribution of flooded pixels depends weakly on the selection of prior value (Giustarini et al., 2016), the noninformative prior value is chosen as $p(F) = p(\overline{F}) = 0.5$, that is, the chance of a pixel being flooded is the same as being non-flooded following Westerhoff et al. (2013). Although this prior value is arbitrary and may impact the results, a sensitivity analysis performed by Guistarini et al. (2016) showed that results remain reliable, in spite. To obtain an estimate of $p(\sigma^0|F)$ and $p(\sigma^0|\overline{F})$ an image segmentation scheme using the fast marching algorithm (FMA) is implemented (Sethian, 1999). Starting from a reference flooded pixel, the FMA provides a computationally efficient approach for coding an image based on grayscale intensities differences concerning the reference pixel. FMA assigns a geodesic distance to each pixel, determining the degree to which each pixel's gray value intensity is like that of the reference pixel. Applying a threshold to this geodesic distance map provides a segmented image. Here we use the MATLAB command "imsegfmm" to perform the FMA based image segmentation with a threshold of 0.05 on the geodesic distance map. Figure S1 shows an example of implementing the algorithm above to the image 20190117150034. Here we select a single reference flooded pixel manually within the water/flooded area, identified visually. A review of the algorithm and applications are provided by Deschamps and Cohen (2001). The SAR image amplitude is shown in Figure S1a, where a water body is visible due to its low intensity. The probabilistic flood map is provided in Figure S1b, where the water body is marked with probabilities near 1, while near-zero values characterize land pixels. Note that there are some pixels with moderate values near areas of high topographic reliefs, which are likely artifacts due to observation noise and the oblique viewing geometry of radar satellites. Figure S1c shows the geodesic distance map calculated for each pixel concerning a reference pixel located within the water body. Applying a threshold of 0.05 to this map yields a segmented image shown in Figure S1d. This binary map roughly divides the image into a flooded and non-flooded pixel, whose histogram is shown as an inset. These histograms are used to obtain an analytical form for $p(\sigma^0|F)$ and $p(\sigma^0|\overline{F})$ used in Equations (1) and (2).

3.3 | Flood exposure analysis

The percent area exposed to flooding is estimated as the pixel area's multiplication with its flooding probability for pixels located within each county or state divided by the county or state area. When more than one SAR acquisition is available for an area within a month, we chose the one with maximum flooding probability for the given month to obtain monthly flood area exposure maps. We only use pixels with a probability larger than 0.75 to calculate the final flooded area percent and exposure maps to reduce the uncertainty due to pixels with low probability. We selected the threshold value by try and error for flood exposure analysis, so mostly flooded pixels are selected, compared with independent datasets such as optical images of flooding areas. This selection allows mitigating the uncertainty in flood exposure maps due to the inclusion of pixels that are not significantly flooded or are affected by considerable speckle noise.

Next, the population exposure is calculated by multiplying each county or state's percent area exposure values with their population, assuming a uniform population distribution. Here we focus on exposure as an intersection of hazard, flooding probability map, and the population distribution. However, hazard and population interactions (vulnerability) to produce risk (Kron, 2005) are not considered in this article. Despite the high-resolution flooding maps obtained from SAR, our analysis is limited to exposure analysis at the state and county level due to the lack of high-resolution census datasets for Iran. Therefore, our study demonstrates the usefulness of SAR-based flood extent mapping and its full capacity yet to be tested for assessing high spatiotemporal flooding exposure.

4 | RESULTS

4.1 | Rainfall change point and trend analysis

Figure 3a shows the distribution of the p-value for Pettitt's test obtained for the time series of monthly

precipitation at each TRMM tile. The tiles with significant *p*-value ≤0.01, 0.05, and 0.1 are color-coded (blue, purple, and red, respectively) in Figure 3b, indicating the TRMM tiles where the null hypothesis is rejected, and thus a change point exists in the mean of a precipitation time series. The white color indicates tiles with *p*-values >0.1 meaning not significant for our study purpose. Some of the TRMM tiles in the wet regions to the north and arid areas in the southeast are characterized by a statistically significant change in their long-term precipitation patterns. Next, we apply Mann–Kendall's test to investigate the presence of a statistically significant precipitation trend at each TRMM tile. Figure 3c shows tiles color-coded to significant pixels with *p*-value ≤0.01, 0.05, and 0.1 and the white color indicates tiles with *p*-value >0.1, for which null hypothesis passes and the term is insignificant. Figure 3d shows the binary trend map distribution, classifying tiles into increasing or decreasing trends. Tiles marked by a red box in Figure 3c,d indicate that significant trends in rainfall are observed. The rainfall decreases through time at various significance levels denoted by blue, dark blue, and red in the northern part of the country. In contrast, a significant upward trend is present in the southeast. Compared with Figure 3b, we find a good correspondence between tiles with change points and those with a significant trend, namely, tiles with a strong precipitation trend are those that have changed their precipitation behavior over the past two decades. Notably, the northern titles experience a decreasing trend (blue pixels), whereas an increasing precipitation trend characterizes those in the southeast (purple pixels) in the arid and semiarid regions of the study area, marked by red boxes.

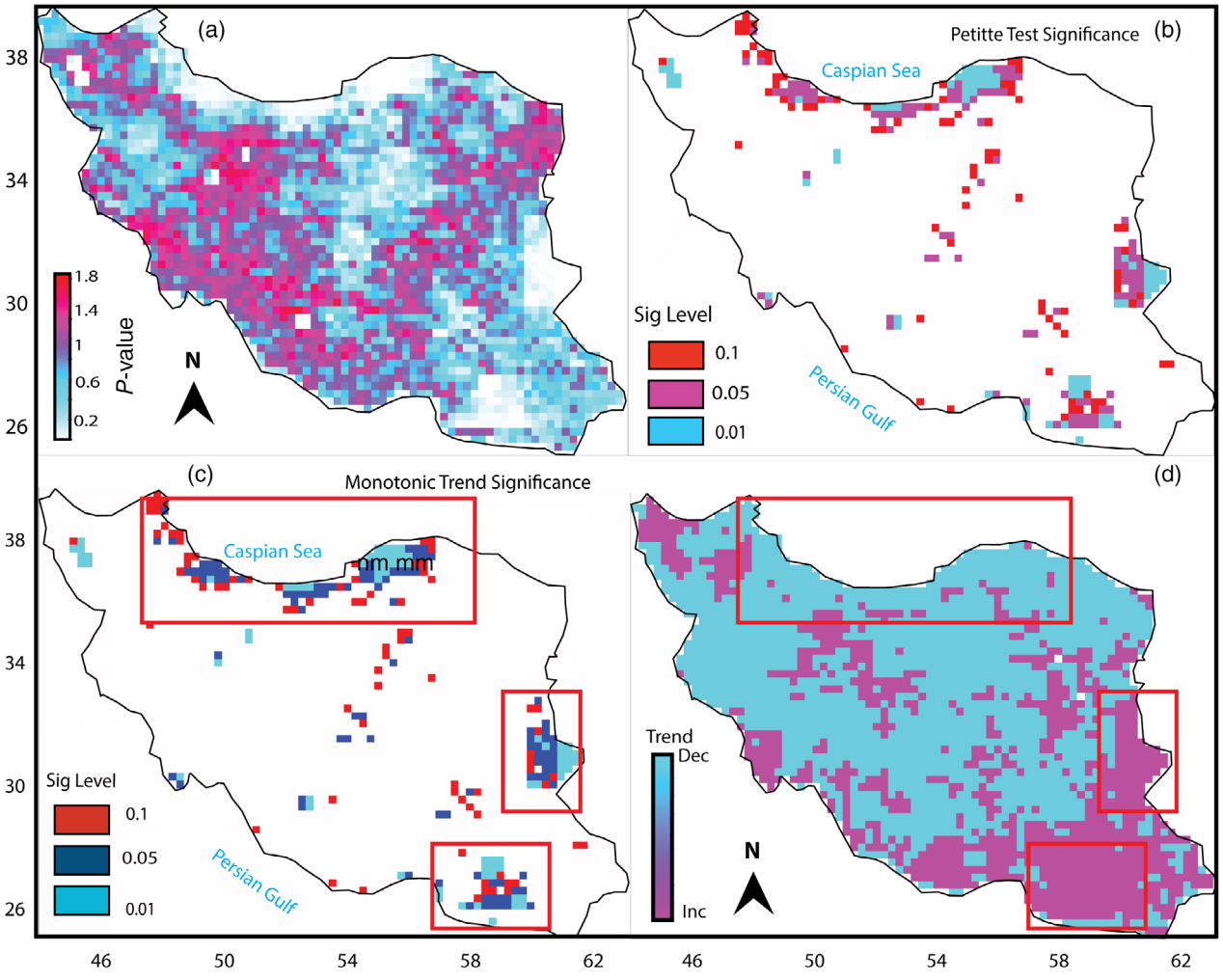

FIGURE 3 (a,b) Pettitt's test of change point. Distribution of *p*-value for time series of monthly precipitation data from 1999 to 2019 estimated for each TRMM tile (a) and the tile with significant *p*-value\le0.1 (b). (c,d) Mann–Kendal test for a monotonic trend. Significance level analysis for the existence of a monotonic trend in Iran's monthly precipitation data from 1999 to 2019 at different significance levels (c) and trend map showing increasing or decreasing pattern in precipitation for the same period (d). The red box highlights the trend and significance areas

4.2 | Probabilistic flood extent and exposure analysis

Figure S2 shows examples of probabilistic flood maps obtained for four SAR images of frame 96 acquired at January 16, 2019 14:18:37, February 2, 2019 14:18:36, February 21, 2019 14:18:36, and March 5, 2019 14:18:36 over the Dasht-e Kavir, a large desert within the Iran Plateau, where no permanent water body exit. The maps show the extent of flooding caused by the unprecedented precipitation as SAR pixels with significant marginal probability. The extent of the major flooded area to the northeast changes slightly across these images, indicating the effect of precipitation and flooding. The southwest's minor L-shaped flooded area varies in size, highlighted by SAR pixels with a reduced flooding probability. Further, the probabilistic flood maps for the 673 SAR images spanning January to March 2019 are provided in an online repository mentioned in the acknowledgment.

Figure 4 shows maps of monthly flood exposed area percent at state and county levels for January through March 2019. The main results of flooded area percentage, flood exposed population number, and precipitation (mm) value in January, February, and March are reported in Table 1. We found 22 states that more than 15% of their area was flooded in January, 9 states in February, and 15 states in March. High flooded area percent is observed in the northwestern and southeastern parts of the country (Figure 4). Among states, Qazvin experienced the highest flooding percent of 36% in January, while 32% and 27% of the Kurdistan areas were flooded in February and March. Furthermore, 71, 36, and 44 counties were flooded more than 30%, and 9, 2, and 2 counties were flooded more than 50% in January, February, and March. Takestan, with a flooded area percent of 73% in January, experienced the worst conditions among counties. Overall, January and March were characterized by the most extensive flooding.

Monthly population exposure to flooding at the state and county level for January, February, and March 2019 are also shown in Figure 5, and the highlights are reported in Table 1. Our analysis shows that, over the entire country, about 15 million people were exposed to flood in January, with more than 2.1 and 1.6 million people in Tehran and Razavi Khorasan states alone. Furthermore, 11.3 million and 11.3 million were exposed in February and March, respectively, with the highest exposed population of 1.4 million and 1.6 million in

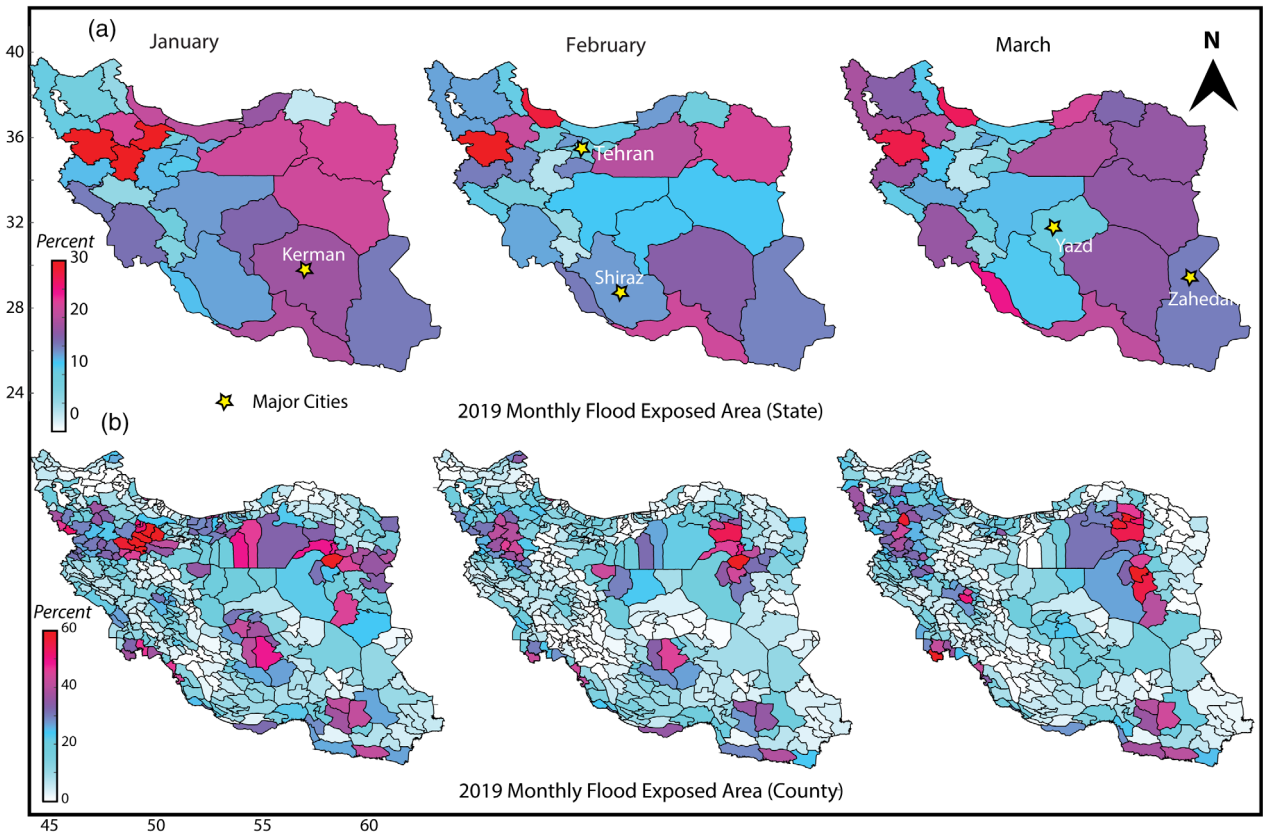

FIGURE 4 The 2019 monthly flooding area exposure percentile in state level (a) and county (b). January, February, and March 2019 months are presented here. Note that the color bars in the panel (a) and (b) are different

TABLE 1 Summary of results from flood exposure analysis presented in this study

		January				February				March			
		Number				Number				Number			
Variables	**Country level**	**Max. value**	**>15% count**	**>30% count**	**>50% count**	**Max. value**	**>15% count**	**>30% count**	**>50% count**	**Max. value**	**>15% count**	**>30% count**	**>50% count**
Flooded area	State	36% *Qazvin*	22	2	0	32% *Kurdistan*	9	1	0	27% *Kurdistan*	15	0	0
	County	73% *Takestan*	168	71	9	65% *Bajestan*	120	36	2	38% *Abadan*	128	44	9
Flood exposed population		Max	$>3 \times 10^5$ count	$>5 \times 10^5$ count	$>1 \times 10^6$ count	Max	$>3 \times 10^5$ count	$>5 \times 10^5$ count	$>1 \times 10^6$ count	Max.	$>3 \times 10^5$ count	$>5 \times 10^5$ count	$>1 \times 10^6$ count
	State	2.1×10^6 *Tehran*	18	9	2	1.4×10^6 *Razavi Khorasan*	14	9	2	1.1×10^6 *Razavi Khorasan*	16	9	1
	County	0.82×10^6 Tehran	4	1	–	0.58×10^6 Tehran	2	1	–	0.96×10^6 Tehran	1	1	–
Precipitation		Max.	>80 mm	>150 mm	>200 mm	Max.	>80 mm	>150 mm	>200	Max value	>80 mm	>150 mm	>200 mm
	State	219 mm *Kohgiluyeh and Boyer*	8	3	1	101 mm "*Kohgiluyeh and Boyer-Ahmad*"	1	–	1	214 mm *Lorestan*	18	5	1
	County	258 mm *Charam*	119	40	14	184 mm *Taybad*	44	2	–	242 mm *Poldokhtar*	234	73	10

Note: The summary includes flooded area percentages, flood exposed population, and precipitation (mm) value in January, February, and March 2019 for counties and states. The states and counties most affected by flooding are highlighted in this table and shown in Figure 1.

Razavi Khorasan state (Table 1). The results from a detailed analysis of flooded area percentage and population exposure for all the states and counties as well as the associated precipitation for January, February, and March, of 2019 are provided in an online repository with a link given in acknowledgment.

5 | DISCUSSION

We conducted an extensive analysis of the area and population exposed to Iran's 2019 flood, using the entire archive (673 images) of Sentinel-1 data. We applied a fast-marching algorithm combined with a Bayesian inference scheme and assigned to SAR pixels a flooding probability. SAR-based Bayesian approach was able to characterize uncertainty associate with each pixel class. Furthermore, this exercise provides vital information on flood extent and exposure that are not often available by analyzing optical imageries due to cloud cover. For validation purposes, an available optical dataset is shown in Figure S3. In the lower panel, Landsat 8 (bands 6–5–3) imagery acquired during January 7, February 24, and March 12, 2019, are shown, highlighting water bodies in dark blue. The corresponding SAR-based probabilistic flood maps for similar dates are also shown in the upper panel, Figure S3. We find a good agreement between the two datasets. In our earlier study, Sherpa et al. (2020) thoroughly validated the SAR-based probabilistic flood mapping algorithm against independent datasets and found results consistent with that of other publications (Giustarini et al., 2016; Schlaffer et al., 2017). We acknowledge that effects such as wind-induced roughening and SAR oblique incidence angle may reduce waterbody classification accuracy. A mask can be developed based on an available digital elevation model and SAR viewing geometry to mitigate these effects and identify and remove pixels affected by shadow, layover, or foreshortening effects. Furthermore, a consistency verification step can be applied, which exploits the idea that neighboring pixels should be treated similarly in terms of flooding probability and thus reduces the effect of localized noise such as wind-roughening. Such rigorous analysis is required when dealing with flood exposure at high resolutions. However, for the county and state-level exposure assessments done here, these corrections are not

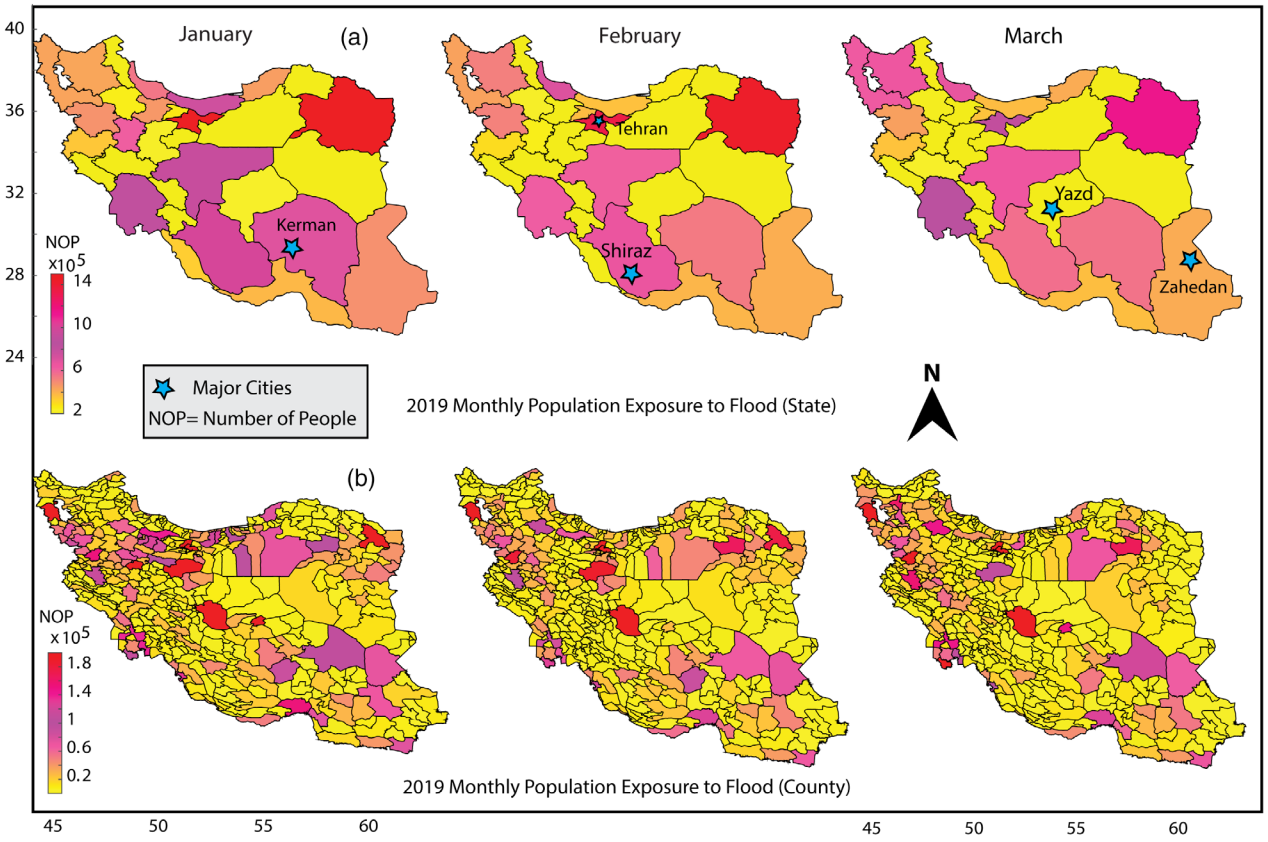

FIGURE 5 The 2019 monthly flooding population exposure map in state and county level for January, February, and March. Note that the color bars in the panel (a) and (b) are different

applied, and the overall impact of such localized nuisance is minimal in the overall result. We showed that flood exposure analysis could be performed at the state and county level using the mapped flood extent, determined by the available coarse census data. However, if the higher resolution census datasets become available, our analysis can be readily expanded to a much higher resolution. As for the uncertainty assessments, note that the Bayesian approach is employed to estimate uncertainty for flooding levels at each pixel. Thus a pixel with a larger flooding probability is more likely to be flooded than a pixel with a low probability. We also selected pixels with a probability larger than 0.75 for the exposure analysis, reducing the uncertainty from pixels with moderate and low probability values.

Extreme precipitation events are likely to increase by warming climate with significant frequency changes (AghaKouchak et al., 2020). The precipitation data based on NASA's TRMM products were analyzed using several statistical tests to understand the study area's precipitation patterns. We found high monthly precipitation compared with the 20-year monthly average from October 2018 to March 2019, indicating intensified wet season in years over the study area. We show that many states and counties receive more than 80 and 150 mm precipitation in January through March 2019. Our analysis showed that over the past 20 years, contrasting precipitation patterns affected parts of Iran with a significant decreasing precipitation trend in the north and northeast and a significant increasing precipitation trend in the south and southeast. Modarres and Sarhadi (2009) used ground-based measurements and showed increasing and decreasing trends, where negative trends of annual rainfall characterize northern and northwestern regions. In contrast, positive trends affect the arid and semiarid regions of Iran. Further, Alizadeh-Choobari and Najafi (2018) suggested that heavy precipitation frequency changes depending on the geographical location when considering warming climate conditions. Vaghefi et al. (2019) predicted a rise of up to 100 mm yr^{-1} in the Mediterranean and Semi-Desert climates and the Caspian zones and a modest increase in the central Cold Semi-Deserts using RCP4.5. Also indicating the wet regions of the country get wetter, while the dry areas get drier, which is also suggested by Abbaspour et al. (2009). On the other hand, a significant decrease in the precipitation of about 100 mm yr^{-1} in the Hot Semi-Desert areas and a relatively stable Caspian zone climate using climate scenario of RCP8.5 in concluded by the same study (Vaghefi et al., 2019).

In addition, various studies have shown increasing and contrasting flood patterns in recent years around the globe linked to various climatic, environmental, and anthropogenic factors. A study by Blöschl et al. (2019) showed an increase in flood discharges in northwestern Europe with decreasing pattern in the stream gauges in southern and eastern Europe. Further, an increase in the frequency of flood events is observed by Slater and Villarini (2016) in the central United States, whereas a decreasing trend is observed in the southeastern part of the united states. Globally, an increasing trend in the magnitude and frequency of floods was reported by Berghuijs et al. (2017) from 1980 to 2009 with the largest changes in Europe and the United States. Extreme rainfall-related flooding is reported in India in the recent year of 2019 (Mishra et al., 2018; Sherpa et al., 2020). Furthermore, Vaghefi et al. (2019) anticipated an increase in Iran's climate extremes, including extended periods of maximum temperature, dry and wet conditions, and extended dry periods interrupted by intermittent heavy rainfalls, intensifying flooding.

The 2019 flood was ranked the second most costly event in Iran's flooding history and led to more than 15 million exposure in January and 11 million in February March to 2019 flood. An increase in the frequency and intensity of such flooding events is anticipated within the coming years (Hoegh-Guldberg et al., 2018). In addition, human activities, and interventions such as deforestation, urbanization, water management infrastructures, and modification of channels or river flow regulations could attenuate extreme events (Familkhalili & Talke, 2016; Hajian et al., 2019; Ralston et al., 2019; Talke et al., 2018) alongside with geographical location or soil type or terrain which is also the major case in locations like Iran where geophysical condition and climate conditions induce flooding. Further, Hajian et al. (2019), highlighted that even in the absence of deforestation, climate change such as extreme rainfall presents a significant flood hazard in the northern province of Iran around the Caspian sea.

6 | CONCLUSIONS

This study investigated a climate extreme, that is, heavy precipitation, and the associated flooding in Iran using high-resolution ESA SAR and NASA TRMM data. We also quantified the human exposure to climate events and analyzed trends in monthly precipitation. Significant increasing in the northern and decreasing precipitation patterns in south and southwest regions of the study area are observed during 1999–2019, with significant precipitation during October 2018 to March 2019, well above the long-term averages. We applied fast marching algorithm approach for segmenting SAR images into flooded and non-flooded pixels and applied

a Bayesian framework to generate probabilistic maps of flooding extent and exposure maps for January, February, and March of 2019 over the entire country of Iran. The generated maps are not impacted by cloud cover and provide information on flooding conditions independent from daylight and also provides uncertainty associated with each pixel.

We observed high flooded area percent in the northwestern and southeastern parts of the country, with 22 states that more than 15% of their area was flooded in January, 9 states in February, and 15 states in March in the entire country. Our monthly population exposure analysis to flooding at the state and county level showed the exposure of 15 million people to flood in January, 11.3 million and 11.3 million in February and March. Our analysis indicates the potential use of the Sentinel-1 SAR dataset and probabilistic flood maps for flood exposure analysis during extreme rainfall events where ground access may not be feasible.

Adaptation decision-making in response to climate extremes causing flooding requires an enhanced understanding of physical and environmental hazards, future exposure to hazards, social perceptions of risk, and understanding the legal environment that facilitates or obstructs adaptation strategies. The datasets provided here give a direct measure of disasters' socioeconomic impact. They also can constrain physical models used for future projections of flooding extent. Thus, our SAR-based flood extent and exposure maps are critical components of effective adaptation decision-making in the era of climate change that extreme events are becoming a norm.

ACKNOWLEDGMENTS

The work of Sonam Futi Sherpa and Manoochehr Shirzaei was supported in part by NASA Grant 80NSSC170567. Sentinel-1 A/B data are available at https://vertex.daac.asf.alaska.edu/. The population data are obtained from https://data.humdata.org. Daily TRMP precipitation data are available at https://pmm.nasa.gov/data-access/downloads/trmm). The supplementary link to the google drive folder is found here https://drive.google.com/drive/u/0/folders/1kM0lO28D4twX2pAEWQtcTZJBtj87Gtt_. The authors thank Jui-Chi Lee for assistance in generating supplementary flood maps.

DATA AVAILABILITY STATEMENT

Data sharing is not applicable to this article as no new data were created or analyzed in this study.

ORCID

Sonam Futi Sherpa https://orcid.org/0000-0002-3415-576X

REFERENCES

Abbaspour, K. C., Faramarzi, M., Ghasemi, S. S., & Yang, H. (2009). Assessing the impact of climate change on water resources in Iran. *Water Resources Research*, *45*(10), W10434. https://doi.org/10.1029/2008WR007615

Adnan, M. S. G., Abdullah, A. Y. M., Dewan, A., & Hall, J. W. (2020). The effects of changing land use and flood hazard on poverty in coastal Bangladesh. *Land Use Policy*, *99*, 104868. https://doi.org/10.1016/j.landusepol.2020.104868

AghaKouchak, A., Chiang, F., Huning, L. S., Love, C. A., Mallakpour, I., Mazdiyasni, O., Moftakhari, H., Papalexiou, S. M., Ragno, E., & Sadegh, M. (2020). Climate extremes and compound hazards in a warming world. *Annual Review of Earth and Planetary Sciences*, *48*(1), 519–548. https://doi.org/10.1146/annurev-earth-071719-055228

Alizadeh-Choobari, O., & Najafi, M. S. (2018). Extreme weather events in Iran under a changing climate. *Climate Dynamics*, *50*(1), 249–260. https://doi.org/10.1007/s00382-017-3602-4

Alvan Romero, N., Cigna, F., & Tapete, D. (2020). ERS-1/2 and Sentinel-1 SAR data mining for flood hazard and risk assessment in Lima, Peru. *Applied Sciences*, *10*(18), 6598. https://doi.org/10.3390/app10186598

Bates, P. D., Horritt, M. S., & Fewtrell, T. J. (2010). A simple inertial formulation of the shallow water equations for efficient two-dimensional flood inundation modelling. *Journal of Hydrology*, *387*, 33–45. https://doi.org/10.1016/j.jhydrol.2010.03.027

Bazi, Y., Bruzzone, L., & Melgani, F. (2005). An unsupervised approach based on the generalized Gaussian model to automatic change detection in multitemporal SAR images. *IEEE Transactions on Geoscience and Remote Sensing*, *43*(4), 874–887. https://doi.org/10.1109/TGRS.2004.842441

Berghuijs, W. R., Aalbers, E. E., Larsen, J. R., Trancoso, R., & Woods, R. A. (2017). Recent changes in extreme floods across multiple continents. *Environmental Research Letters*, *12*(11), 114035. https://doi.org/10.1088/1748-9326/aa8847

Blöschl, G., Hall, J., Viglione, A., Perdigão, R. A. P., Parajka, J., Merz, B., Lun, D., Arheimer, B., Aronica, G. T., Bilibashi, A., Boháč, M., Bonacci, O., Borga, M., Čanjevac, I., Castellarin, A., Chirico, G. B., Claps, P., Frolova, N., Ganora, D., … Živković, N. (2019). Changing climate both increases and decreases European river floods. *Nature*, *573*(7772), 108–111. https://doi.org/10.1038/s41586-019-1495-6

Bodian, A., Diop, L., Panthou, G., Dacosta, H., Deme, A., Dezetter, A., Ndiaye, P. M., Diouf, I., & Vischel, T. (2020). Recent trend in hydroclimatic conditions in the Senegal river basin. *Water*, *12*(2), 436. https://doi.org/10.3390/w12020436

Chini, M., Hostache, R., Giustarini, L., & Matgen, P. (2017). A hierarchical split-based approach for parametric thresholding of SAR images: Flood inundation as a test case. *IEEE Transactions on Geoscience and Remote Sensing*, *55*(12), 6975–6988. https://doi.org/10.1109/TGRS.2017.2737664

Chini, M., Pulvirenti, L., & Pierdicca, N. (2012). Analysis and interpretation of the COSMO-SkyMed observations of the 2011 Japan tsunami. *IEEE Geoscience and Remote Sensing Letters*, *9*(3), 467–471. https://doi.org/10.1109/LGRS.2011.2182495

Clement, M. A., Kilsby, C. G., & Moore, P. (2018). Multi-temporal synthetic aperture radar flood mapping using change detection: Multi-temporal SAR flood mapping using change detection.

Journal of Flood Risk Management, *11*(2), 152–168. https://doi.org/10.1111/jfr3.12303

Coumou, D., & Rahmstorf, S. (2012). A decade of weather extremes. *Nature Climate Change*, *2*(7), 491–496. https://doi.org/10.1038/nclimate1452

Darand, M., Amanollahi, J., & Zandkarimi, S. (2017). Evaluation of the performance of TRMM multi-satellite precipitation analysis (TMPA) estimation over Iran. *Atmospheric Research*, *190*, 121–127. https://doi.org/10.1016/j.atmosres.2017.02.011

Deschamps, T., & Cohen, L. D. (2001). Fast extraction of minimal paths in 3D images and applications to virtual endoscopy. *Medical Image Analysis*, *5*(4), 281–299. https://doi.org/10.1016/s1361-8415(01)00046-9

di Mauro, C., Hostache, R., Matgen, P., Pelich, R., Chini, M., van Leeuwen, P. J., Nichols, N. K., & Blöschl, G. (2021). Assimilation of probabilistic flood maps from SAR data into a hydrologic-hydraulic forecasting model: A proof of concept. *Hydrology and Earth System Sciences Discussions*, *25*(7), 4081–4097. https://doi.org/10.5194/hess-25-4081-2021

Dong, J., Crow, W. T., Duan, Z., Wei, L., & Lu, Y. (2019). A double instrumental variable method for geophysical product error estimation. *Remote Sensing of Environment*, *225*, 217–228. https://doi.org/10.1016/j.rse.2019.03.003

Dottori, F., Szewczyk, W., Ciscar, J.-C., Zhao, F., Alfieri, L., Hirabayashi, Y., Bianchi, A., Mongelli, I., Frieler, K., Betts, R. A., & Feyen, L. (2018). Increased human and economic losses from river flooding with anthropogenic warming. *Nature Climate Change*, *8*(9), 781–786. https://doi.org/10.1038/s41558-018-0257-z

Duan, Z., Tuo, Y., Liu, J., Gao, H., Song, X., Zhang, Z., Yang, L., & Mekonnen, D. F. (2019). Hydrological evaluation of open-access precipitation and air temperature datasets using SWAT in a poorly gauged basin in Ethiopia. *Journal of Hydrology*, *569*, 612–626. https://doi.org/10.1016/j.jhydrol.2018.12.026

Elkhrachy, I., Pham, Q. B., Costache, R., Mohajane, M., Rahman, K. U., Shahabi, H., Linh, N. T. T., & Anh, D. T. (2021). Sentinel-1 remote sensing data and hydrologic engineering centres river analysis system two-dimensional integration for flash flood detection and modelling in new Cairo city, Egypt. *Journal of Flood Risk Management*, *14*(2), e12692. https://doi.org/10.1111/jfr3.12692

Familkhalili, R., & Talke, S. A. (2016). The effect of channel deepening on tides and storm surge: A case study of Wilmington, NC. *Geophysical Research Letters*, *43*(17), 9138–9147. https://doi.org/10.1002/2016GL069494

Farr, T. G., Rosen, P. A., Caro, E., Crippen, R., Duren, R., Hensley, S., Kobrick, M., Paller, M., Rodriguez, E., Roth, L., Seal, D., Shaffer, S., Shimada, J., Umland, J., Werner, M., Oskin, M., Burbank, D., & Alsdorf, D. (2007). The shuttle radar topography mission. *Reviews of Geophysics*, *45*(2), RG2004. https://doi.org/10.1029/2005RG000183

FloodList. (2018). https://floodlist.com/asia/iran-flash-floods-august-2017

Gao, H., Birkel, C., Hrachowitz, M., Tetzlaff, D., Soulsby, C., & Savenije, H. H. G. (2019). A simple topography-driven and calibration-free runoff generation module. *Hydrology and Earth System Sciences*, *23*(2), 787–809. https://doi.org/10.5194/hess-23-787-2019

Giustarini, L., Hostache, R., Kavetski, D., Chini, M., Corato, G., Schlaffer, S., & Matgen, P. (2016). Probabilistic flood mapping using synthetic aperture radar data. *IEEE Transactions on Geoscience and Remote Sensing*, *54*(12), 6958–6969.

Giustarini, L., Vernieuwe, H., Verwaeren, J., Chini, M., Hostache, R., Matgen, P., Verhoest, N. E. C., & De Baets, B. (2015). Accounting for image uncertainty in SAR-based flood mapping. *International Journal of Applied Earth Observation and Geoinformation*, *34*, 70–77. https://doi.org/10.1016/j.jag.2014.06.017

Giustarini, L., Hostache, R, Kavetski, D., Chini, M., Corato, G., Schlaffer, S., & Matgen, P. (2016). Probabilistic flood mapping using synthetic aperture radar data. *IEEE Transactions on Geoscience and Remote Sensing*, *54*(12), 6948–6969.

Hajian, F., Dykes, A. P., & Cavanagh, S. (2019). Assessment of the flood hazard arising from land use change in a forested catchment in northern Iran. *Journal of Flood Risk Management*, *12*(4), e12481. https://doi.org/10.1111/jfr3.12481

Hamed, K. H. (2008). Trend detection in hydrologic data: The Mann–Kendall trend test under the scaling hypothesis. *Journal of Hydrology*, *349*(3), 350–363. https://doi.org/10.1016/j.jhydrol.2007.11.009

Henderson, F. M., & Lewis, A. J. (1998). Principles and applications of imaging radar. In F. M. Henderson & A. J. Lewis (Eds.), *Manual of remote sensing* (3rd ed.). John Wiley and Sons, Inc..

Hirabayashi, Y., Kanae, S., Emori, S., Oki, T., & Kimoto, M. (2008). Global projections of changing risks of floods and droughts in a changing climate. *Hydrological Sciences Journal*, *53*(4), 754–772. https://doi.org/10.1623/hysj.53.4.754

Hirabayashi, Y., Tanoue, M., Sasaki, O., Zhou, X., & Yamazaki, D. (2021). Global exposure to flooding from the new CMIP6 climate model projections. *Scientific Reports*, *11*(1), 3740. https://doi.org/10.1038/s41598-021-83279-w

Hirsch, R. M., & Slack, J. R. (1984). A nonparametric trend test for seasonal data with serial dependence. *Water Resources Research*, *20*(6), 727–732. https://doi.org/10.1029/WR020i006p00727

Hoegh-Guldberg, O., Jacob, D., Bindi, M., Brown, S., Camilloni, I., Diedhiou, A., Djalante, R., Ebi, K., Engelbrecht, F., & Guiot, J. (2018). Impacts of 1.5°C global warming on natural and human systems. Global Warming of 1.5°C. An IPCC Special Report.

Huffman, G. J., Adler, R. F., Bolvin, D. T., & Nelkin, E. J. (2010). The TRMM multi-satellite precipitation analysis (TMPA). In *Satellite rainfall applications for surface hydrology* (pp.3–22). Dordrecht, Netherlands: Springer. https://doi.org/10.1007/978-90-481-2915-7_1

Huffman, G. J., Bolvin, D. T., Nelkin, E. J., Wolff, D. B., Adler, R. F., Gu, G., Hong, H., Bowman, K. P., & Stocker, E. F. (2007). The TRMM Multisatellite Precipitation Analysis (TMPA): Quasi-global, multiyear, combined-sensor precipitation estimates at fine scales. *Journal of Hydrometeorology*, *8*(1), 38–55.

Intergovernmental Panel on Climate Change. (2014). *Climate Change 2013 – The Physical Science Basis: Working Group I Contribution to the Fifth Assessment Report of the Intergovernmental Panel on Climate Change*. Cambridge University Press. https://doi.org/10.1017/CBO9781107415324

Kendall, M. G. (1975). *Rank Correlation Methods*, 4th edition. London: Charles Griffin.

Kron, W. (2005). Flood risk = hazard*values*vulnerability. *International Water Resources Association*, *30*, 58–68.

Kummerow, C., Barnes, W., Kozu, T., Shiue, J., & Simpson, J. (1998). The tropical rainfall measuring mission (TRMM) sensor package. *Journal of Atmospheric and Oceanic Technology*, *15*(3), 809–817. https://doi.org/10.1175/1520-0426(1998)015<0809:TTRMMT>2.0.CO;2

Malnes, E., Guneriussen, T., & Høgda, K. A. (2002). Mapping of flood-area by Radarsat in Vansjø, Norway. Proceedings of the geomatics in the era of radarsat, 1997, Ottawa, Canada.

Mann, H. B. (1945). Nonparametric tests against trend. *Econometrica*, *13*(3), 245–259. https://doi.org/10.2307/1907187

Mason, D. C., Schumann, G. J.-P., Neal, J. C., Garcia-Pintado, J., & Bates, P. D. (2012). Automatic near real-time selection of flood water levels from high resolution synthetic aperture radar images for assimilation into hydraulic models: A case study. *Remote Sensing of Environment*, *124*, 705–716. https://doi.org/10.1016/j.rse.2012.06.017

Matgen, P., Hostache, R., Schumann, G., Pfister, L., Hoffmann, L., & Savenije, H. H. G. (2011). Towards an automated SAR-based flood monitoring system: Lessons learned from two case studies. *Physics and Chemistry of the Earth, Parts A/B/C*, *36*(7), 241–252. https://doi.org/10.1016/j.pce.2010.12.009

Matgen, P., Schumann, G., Henry, J.-B., Hoffmann, L., & Pfister, L. (2007). Integration of SAR-derived river inundation areas, high-precision topographic data and a river flow model toward near real-time flood management. *International Journal of Applied Earth Observation and Geoinformation*, *9*(3), 247–263. https://doi.org/10.1016/j.jag.2006.03.003

Mishra, V., Aaadhar, S., Shah, H., Kumar, R., Pattanaik, D. R., & Tiwari, A. D. (2018). The Kerala flood of 2018: Combined impact of extreme rainfall and reservoir storage. *Hydrology and Earth System Sciences Discussions*, 1–13. https://doi.org/10.5194/hess-2018-480

Modarres, R., & Sarhadi, A. (2009). Rainfall trends analysis of Iran in the last half of the twentieth century. *Journal of Geophysical Research: Atmospheres*, *114*, D03101. https://doi.org/10.1029/2008JD010707

Neal, J., Schumann, G., & Bates, P. (2012). A subgrid channel model for simulating river hydraulics and floodplain inundation over large and data sparse areas. *Water Resources Research*, *48*(11), W11506. https://doi.org/10.1029/2012WR012514

Nico, G., Pappalepore, M., Pasquariello, G., Refice, A., & Samarelli, S. (2000). Comparison of SAR amplitude vs. coherence flood detection methods—A GIS application. *International Journal of Remote Sensing*, *21*(8), 1619–1631. https://doi.org/10.1080/014311600209931

Oberstadler, R., Hönsch, H., & Huth, D. (1997). Assessment of the mapping capabilities of ERS-1 SAR data for flood mapping: A case study in Germany. *Hydrological Processes*, *11*(10), 1415–1425. https://doi.org/10.1002/(SICI)1099-1085(199708)11:10<1415::AID-HYP532>3.0.CO;2-2

Ouhamdouch, S., & Bahir, M. (2017). Climate change impact on future rainfall and temperature in semi-arid areas (Essaouira Basin, Morocco). *Environmental Processes*, *4*(4), 975–990. https://doi.org/10.1007/s40710-017-0265-4

Pal, S. C., Das, B., Malik, S., Shit, M., & Chakrabortty, R. (2021). Flood frequency analysis and its Management in Selected Part of Bardhaman District, West Bengal. In A. Rukhsana, A. A. Haldar, & L. Satpati (Eds.), *Habitat, ecology and ekistics: Case studies of human-environment interactions in India* (pp. 225–246). Springer International Publishing. https://doi.org/10.1007/978-3-030-49115-4_13

Pettitt, A. N. (1979). A non-parametric approach to the change-point problem. *Journal of the Royal Statistical Society: Series C (Applied Statistics)*, *28*(2), 126–135. https://doi.org/10.2307/2346729

Pulvirenti, L., Chini, M., Pierdicca, N., & Boni, G. (2016). Use of SAR data for detecting floodwater in urban and agricultural areas: The role of the Interferometric coherence. *IEEE Transactions on Geoscience and Remote Sensing*, *54*(3), 1532–1544. https://doi.org/10.1109/TGRS.2015.2482001

Pulvirenti, L., Pierdicca, N., Chini, M., & Guerriero, L. (2013). Monitoring flood evolution in vegetated areas using COSMO-SkyMed data: The Tuscany 2009 case study. *IEEE Journal of Selected Topics in Applied Earth Observations and Remote Sensing*, *6*(4), 1807–1816. https://doi.org/10.1109/JSTARS.2012.2219509

Rahman, M., Ningsheng, C., Mahmud, G. I., Islam, M. M., Pourghasemi, H. R., Ahmad, H., Habumugisha, J. M., Washakh, R. M. A., Alam, M., Liu, E., Han, Z., Ni, H., Shufeng, T., & Dewan, A. (2021). Flooding and its relationship with land cover change, population growth, and road density. *Geoscience Frontiers*, *12*(6), 101224. https://doi.org/10.1016/j.gsf.2021.101224

Ralston, D. K., Talke, S., Geyer, W. R., Al-Zubaidi, H. A. M., & Sommerfield, C. K. (2019). Bigger tides, less flooding: Effects of dredging on barotropic dynamics in a highly modified estuary. *Journal of Geophysical Research: Oceans*, *124*(1), 196–211. https://doi.org/10.1029/2018JC014313

Rogger, M., Agnoletti, M., Alaoui, A., Bathurst, J. C., Bodner, G., Borga, M., Chaplot, V., Gallart, F., Glatzel, G., Hall, J., Holden, J., Holko, L., Horn, R., Kiss, A., Kohnová, S., Leitinger, G., Lennartz, B., Parajka, J., Perdigão, R., … Blöschl, G. (2017). Land use change impacts on floods at the catchment scale: Challenges and opportunities for future research. *Water Resources Research*, *53*(7), 5209–5219. https://doi.org/10.1002/2017WR020723

Rosen, J. (2021). Shifting ground. *Science*, *371*(6532), 876–880. https://doi.org/10.1126/science.371.6532.876

Roy, P., Chandra Pal, S., Chakrabortty, R., Chowdhuri, I., Malik, S., & Das, B. (2020). Threats of climate and land use change on future flood susceptibility. *Journal of Cleaner Production*, *272*, 122757. https://doi.org/10.1016/j.jclepro.2020.122757

Ruzza, G., Guerriero, L., Grelle, G., Guadagno, F. M., & Revellino, P. (2019). Multi-method tracking of monsoon floods using Sentinel-1 imagery. *Water*, *11*(11), 2289. https://doi.org/10.3390/w11112289

Saghafian, B., Farazjoo, H., Bozorgy, B., & Yazdandoost, F. (2008). Flood intensification due to changes in land use. *Water Resources Management*, *22*(8), 1051–1067. https://doi.org/10.1007/s11269-007-9210-z

Sanyal, J., & Lu, X. X. (2004). Application of remote sensing in flood management with special reference to monsoon Asia: A review. *Natural Hazards*, *33*(2), 283–301. https://doi.org/10.1023/B:NHAZ.0000037035.65105.95

Schlaffer, S., Chini, M., Giustarini, L., & Matgen, P. (2017). Probabilistic mapping of flood-induced backscatter changes in SAR time series. *International Journal of Applied Earth Observation and Geoinformation*, *56*, 77–87. https://doi.org/10.1016/j.jag.2016.12.003

Schumann, G., Matgen, P., & Pappenberger, F. (2008). Conditioning water stages from satellite imagery on uncertain data points. *IEEE Geoscience and Remote Sensing Letters*, *5*(4), 810–813. https://doi.org/10.1109/LGRS.2008.2005646

Scotti, V., Giannini, M., & Cioffi, F. (2020). Enhanced flood mapping using synthetic aperture radar (SAR) images, hydraulic modelling, and social media: A case study of hurricane Harvey (Houston, TX). *Journal of Flood Risk Management*, *13*(4), e12647. https://doi.org/10.1111/jfr3.12647

Seneviratne, S. I., Zhang, X., Adnan, M., Badi, W., Claudine, D., Luca, A. D., Ghosh, S., Iskandar, I., Kossin, J., Lewis, S., Otto, F., Pinto, I., Satoh, M., Vicente-Serrano, S. M., Wehner, M., & Zhou, B. (2021). Weather and climate extreme events in a changing climate. In: Climate change 2021: The physical science basis. contribution of working group I to the sixth assessment report of the intergovernmental panel on climate change.

Serinaldi, F., & Kilsby, C. G. (2014). Rainfall extremes: Toward reconciliation after the battle of distributions. *Water Resources Research*, *50*(1), 336–352. https://doi.org/10.1002/2013WR014211

Serinaldi, F., & Kilsby, C. G. (2015). Stationarity is undead: Uncertainty dominates the distribution of extremes. *Advances in Water Resources*, *77*, 17–36. https://doi.org/10.1016/j.advwatres.2014.12.013

Sethian, J. A. (1999). *Level set methods and fast marching methods: Evolving interfaces in computational geometry, fluid mechanics, computer vision, and materials science*. Cambridge University Press.

Sherpa, S. F., Shirzaei, M., Ojha, C., Werth, S., & Hostache, R. (2020). Probabilistic mapping of august 2018 flood of Kerala, India, using space-borne synthetic aperture radar. *IEEE Journal of Selected Topics in Applied Earth Observations and Remote Sensing*, *13*, 896–913. https://doi.org/10.1109/JSTARS.2020.2970337

Shirzaei, M., Bürgmann, R., & Fielding, E. J. (2017). Applicability of Sentinel-1 terrain observation by progressive scans multitemporal interferometry for monitoring slow ground motions in the San Francisco Bay Area. *Geophysical Research Letters*, *44*(6), 2733–2742. https://doi.org/10.1002/2017GL072663

Shukla, P. R., Skea, J., Calvo Buendia, E., Masson-Delmotte, V., Pörtner, H. O., Roberts, D. C., Zhai, P., Slade, R., Connors, S., & van Diemen, R. (2019). IPCC, 2019: Climate Change and Land: An IPCC special report on climate change, desertification, land degradation, sustainable land management, food security, and greenhouse gas fluxes in terrestrial ecosystems.

Slater, L. J., & Villarini, G. (2016). Recent trends in US flood risk. *Geophysical Research Letters*, *43*(24), 12428–12436.

Smith, A., Bates, P. D., Wing, O., Sampson, C., Quinn, N., & Neal, J. (2019). New estimates of flood exposure in developing countries using high-resolution population data. *Nature Communications*, *10*(1), 1814. https://doi.org/10.1038/s41467-019-09282-y

Talke, S. A., Kemp, A. C., & Woodruff, J. (2018). Relative sea level, tides, and extreme water levels in Boston Harbor from 1825 to 2018. *Journal of Geophysical Research: Oceans*, *123*(6), 3895–3914. https://doi.org/10.1029/2017JC013645

Taylor, C. M., Belušić, D., Guichard, F., Parker, D. J., Vischel, T., Bock, O., Harris, P. P., Janicot, S., Klein, C., & Panthou, G. (2017). Frequency of extreme Sahelian storms tripled since 1982 in satellite observations. *Nature*, *544*(7651), 475–478. https://doi.org/10.1038/nature22069

Tiecke, T. G., Liu, X., Zhang, A., Gros, A., Li, N., Yetman, G., Kilic, T., Murray, S., Blankespoor, B., Prydz, E. B., & Dang, H.-A. H. (2017). Mapping the world population one building at a time. *arXiv*, 1–25.

Townsend, P. A. (2002). Relationships between forest structure and the detection of flood inundation in forested wetlands using C-band SAR. *International Journal of Remote Sensing*, *23*(3), 443–460. https://doi.org/10.1080/01431160010014738

United Nations. (2019). *World population prospects 2019: Data booklet*. UN.

Urs, C. W., Werner, C., Wegmüller, U., Strozzi, T., & Wiesmann, A. (2000). Gamma sar and interferometric processing software. Proceedings of the Ers-Envisat symposium, 1620.

Vaghefi, S. A., Keykhai, M., Jahanbakhshi, F., Sheikholeslami, J., Ahmadi, A., Yang, H., & Abbaspour, K. C. (2019). The future of extreme climate in Iran. *Scientific Reports*, *9*(1), 1464. https://doi.org/10.1038/s41598-018-38071-8

Villarini, G. (2012). Analyses of annual and seasonal maximum daily rainfall accumulations for Ukraine, Moldova, and Romania. *International Journal of Climatology*, *32*(14), 2213–2226. https://doi.org/10.1002/joc.3394

Villarini, G., Smith, J. A., Baeck, M. L., Vitolo, R., Stephenson, D. B., & Krajewski, W. F. (2011). On the frequency of heavy rainfall for the Midwest of the United States. *Journal of Hydrology*, *400*(1–2), 103–120. https://doi.org/10.1016/j.jhydrol.2011.01.027

Villarini, G., & Vecchi, G. A. (2012). Twenty-first-century projections of North Atlantic tropical storms from CMIP5 models. *Nature Climate Change*, *2*(8), 604–607. https://doi.org/10.1038/nclimate1530

Wallemacq, P. (2018). Economic losses, poverty & disasters: 1998-2017. https://www.undrr.org/publication/economic-losses-poverty-disasters-1998-2017

Wegnüller, U., Werner, C., Strozzi, T., Wiesmann, A., Frey, O., & Santoro, M. (2016). Sentinel-1 support in the GAMMA software. *Procedia Computer Science*, *100*, 1305–1312. https://doi.org/10.1016/j.procs.2016.09.246

Westerhoff, R. S., Kleuskens, M. P. H., Winsemius, H. C., Huizinga, H. J., Brakenridge, G. R., & Bishop, C. (2013). Automated global water mapping based on wide-swath orbital synthetic-aperture radar. *Hydrology and Earth System Sciences*, *17*(2), 651–663. https://doi.org/10.5194/hess-17-651-2013

Willis, H. H., Narayanan, A., Fischbach, J. R., Molina-Perez, E., Stelzner, C., Loa, K., & Kendrick, L. (2016). *Current and future exposure of infrastructure in the United States to natural hazards*. RAND.

Wobus, C., Lawson, M., Jones, R., Smith, J., & Martinich, J. (2014). Estimating monetary damages from flooding in the United States under a changing climate. *Journal of Flood Risk Management*, *7*(3), 217–229. https://doi.org/10.1111/jfr3.12043

World Bank (2019). https://climateknowledgeportal.worldbank.org/

Yamazaki, D., Watanabe, S., & Hirabayashi, Y. (2018). Global flood risk modeling and projections of climate change impacts. In *Global flood hazard* (pp. 185–203). American Geophysical Union (AGU). https://doi.org/10.1002/9781119217886.ch11

SUPPORTING INFORMATION

Additional supporting information may be found in the online version of the article at the publisher's website.

How to cite this article: Sherpa, S. F., & Shirzaei, M. (2021). Country-wide flood exposure analysis using Sentinel-1 synthetic aperture radar data: Case study of 2019 Iran flood. *Journal of Flood Risk Management*, e12770. https://doi.org/10.1111/jfr3.12770